Estimating subsurface parameter fields for seismic migration: Velocity model building

Ian F. Jones, ION Geophysical Corporation, e-mail: ian.jones@iongeo.com

Published October 2015. © 2015 SEG, http://dx.doi.org/10.1190/1.9781560803027.entry3.

Abstract

To produce a reliable image of the subsurface, we must use a depth-migration scheme that requires a detailed model of the parameter fields for use by migration. Obtaining reliable values of all parameters for the full 3D volume to be imaged is perhaps impractical, so we make various simplifying assumptions. Even with such assumptions, inverting for a wide range of parameters given a limited and inconsistent data set is challenging. Ray-based tomography supplemented with waveform inversion can yield a suitable model. However, we often still need to fall back on various techniques that require manual intervention to incorporate detailed velocity anomalies into the migration model.

Introduction — What migration sets out to do

Seismic data migration is a procedure which ideally repositions recorded reflection energy back to its true subsurface spatial location to form a reliable subsurface image. The degree to which this is achievable depends on the level of geophysical and algorithmic simplification used in writing the migration algorithm itself.

These simplifications involve two steps: first, selecting a suitable description of how sound waves have propagated in the earth, and second, choosing which numerical scheme to use in computationally implementing the selected description. Examples of the first step might be deciding on a one-way (primaries-only) P-wave viscoacoustic approximation for wave propagation; e.g., we hope to image P-wave energy that has undergone only a single bounce (reflection) while including attenuation (Q) effects.

We might chose to ignore lateral velocity variation over the range of offsets in the recorded data (then referred to as prestack time migration, preSTM) or attempt to accommodate such lateral velocity variation (then referred to as prestack depth migration, preSDM). The numerical scheme we use to implement this choice could be a ray-based scheme (such as Kirchhoff or beam) or perhaps a finite-difference (FD) wavefield-extrapolation migration (WEM) scheme, executed perhaps in the space-time or wavenumber-frequency domains.

For a migration algorithm to function, in addition to the recorded prestack field data, it needs a subsurface parameter field for the entire 3D volume to be imaged. For P-wave reflection energy, this parameter field in the most general sense could include the P-wave velocity (V_P), the associated structural inline and crossline dip field, anisotropy parameters, and attenuation (Q).

As migration technology has evolved over the past 50 years (primarily just keeping up with available computer power, as outlined in Table 1), increasingly elaborate model-estimation techniques have been required. As we relax the restrictive assumptions and simplifications in our representation of wave propagation, so ever more detailed and accurate parameter fields are required.

For example, there is no point in building a very detailed velocity field with many small-scale features with rapid lateral velocity variation if we intend to use a migration approximation that does not comprehend lateral velocity change (e.g., time migration). Conversely, a reverse time migration (RTM) which in principle can deal

3180_Ch01.indd 1 12/10/2015 11:15:55 AM

Table 1. Timeline for evolution of industrial migration techniques. After Jones et al. (2008), Chapter 1: Introduction, Table 1.

Period in use as primary deliverable	Technique	Common domain and type of application (x, t) or (x, y, t) = (space, time), (x, y, z) = (space, depth), (x, f) or (x, y, f) = (space, frequency)
1975–1988	2D postSTM	Finite-difference (FD) (x, t) and (x, f) Initially with 15°, then 45°, and later 60° dip limits
1978–1988	2D DMO + 2D postSTM	Dip moveout (DMO) Introduced to remove some aspects of the dip dependence of velocity prior to stacking
1975–1988	2D postSTM	Finite-difference (FD) (x, t) and (x, f) Initially with 30°, then 45°, and later 60° dip limits
1980–1988	2D postSDM	Finite-difference (FD) (x, f) Initially 45° and later 60° dip limits
1985–1995	3D DMO + 3D postSTM	3D DMO + FD (x, y, f) time migration Initially with 45° and later 60° dip limits
1990–2001	3D DMO + 3D zero-offset constant-velocity preSTM, followed by demigration of the stack and then 3D postSTM	3D DMO + constant-velocity phase-shift (Stolt) zero-offset preSTM and subsequent demigration, in conjunction with FD (x, y, f) postSTM
1990–1995	2D full-offset preSDM	FD focusing analysis interactive (x, f)
1993–1997	DMO + 3D zero-offset constant-velocity preSTM, followed by demigration of the stack and then 3D postSDM	Constant-velocity phase-shift (Stolt) zero-offset preSTM and subsequent poststack demigration, in conjunction with FD (x, y, f) postSDM
1995–present	Full-offset $V(x, y, z)$ 3D preSDM	Kirchhoff (x, y, z) isotropic
2000–2003	Full-offset $V(x, y, t)$ 3D preSTM	Kirchhoff (x, y, t) straight ray
2002–present	Full-offset $V(x, y, t)$ 3D anisotropic preSTM	Kirchhoff (x, y, t) curved and turning ray and anisotropic
2000–present	Full-offset $V(x, y, z)$ 3D preSDM	Isotropic wavefield extrapolation (WE) with, for example, FD, SSFPI, and non-WE beam
2000–present	Full-offset $V(x, y, z)$ 3D anisotropic preSDM outputting gathers	TTI Kirchhoff (x, y, z) anisotropic turning ray
2005–2008	Full-offset $V(x, y, z)$ 3D anisotropic preSDM outputting gathers	VTI wavefield extrapolation with, for example, FD SSFPI and, alternatively, non-WE beam
2006–2009	Full-offset $V(x, y, z)$ 3D anisotropic preSDM	VTI two-way wavefield extrapolation using reverse time migration or two-pass one-way extrapolation
2008–2009	Full-offset $V(x, y, z)$ 3D anisotropic preSDM outputting gathers	VTI beam or two-way wavefield extrapolation using reverse time migration
2009–present	Full-offset $V(x, y, z)$ 3D anisotropic viscoacoustic preSDM outputting gathers	TTI beam or Kirchhoff compensation for attenuation (Q-migration)
2009–present	Full-offset $V(x, y, z)$ 3D anisotropic preSDM outputting gathers	TTI beam or two-way wavefield extrapolation using reverse time migration
2012–present	Full-offset $V(x, y, z)$ 3D anisotropic preSDM outputting gathers	Orthorhombic beam or two-way wavefield extrapolation using reverse time migration

PostSTM = poststack time migration; postSDM = poststack depth migration; preSTM = prestack time migration; preSDM = prestack depth migration; FD migration = finite-difference migration; WE = wavefield extrapolation; SSFPI = split-step Fourier plus interpolation; TTI = tilted transverse isotropy; VTI = vertical transverse isotropy.

with lateral velocity variation on a scale length of just tens of meters will need a high-resolution velocity-estimation technique to furnish a sufficiently detailed velocity model. Otherwise, there would be little point in running the RTM.

It is the obtention of these subsurface geophysical parameters that will be described in this article.

In addition, most algorithms also require specification of migration parameters related to dip response and aperture and in turn, related to cost. Limiting the values of these parameters would reduce cost but degrade the image, so trade-off decisions need to be made in selecting these migration parameter values (e.g., Berkhout, 1982; Robein, 2003).

As an aside, we ideally should use a parameter-model estimation technique that is based on the same level of theoretical and numerical approximations as the migration scheme we intend to use. Otherwise, we will have a mismatch in algorithmic capabilities. Unfortunately, this ideal case has seldom been achieved in the past. In practice, we usually have about a 10-year lag between implementation of a migration scheme and the parameter-estimation technique based on the corresponding level of theoretical complexity.

The reason for this is simple. Migration takes a given set of parameters and produces an image (a "forward" problem), which is easy to do, whereas model building takes the raw unmigrated or migrated data and has to use them in some way to provide parameter estimation (an "inverse" problem), which is very difficult to do. Therefore, as soon as we have enough computer power, we can run complex migration algorithms, but for the corresponding inverse problem, we have a plethora of complex issues to resolve (overdetermined inversion of inconsistent data, local minima, large numbers of internal iterations required to converge, and so forth; e.g., Symes and Huang, 2014; Gerard T. Schuster, personal communication, 2015).

The word *velocity* itself can be contentious. The unwary practitioner can be readily misled by the numerical quantity that happens to have units of meters per second. Is the quantity being considered an instantaneous, interval, average, maximum coherency, stacking, root-mean-square (RMS), normal-moveout (NMO), vertical, horizontal, or polar velocity?

As pointed out by Al-Chalabi (1997, 2014), it might well be advisable to refer to the numbers we use in migration and data preconditioning as processing velocities, or provelocities, rather than just velocities to distinguish them from the actual sound speed in a given rock volume. Similar confusion can arise when describing geologic depth (as measured in a borehole) as opposed to geophysical depth (as obtained from a depth-migration image). These ideas will be revisited later, in the section on anisotropy.

It is perhaps also worth noting that as velocity estimation needs a prestack domain (to evaluate moveout behavior), then velocity analysis performed in the migrated domain will require migrated gathers. Whereas ray methods such as Kirchhoff and beam migration can inherently produce gathers, wavefield-extrapolation methods do not. In the case of WEM methods, we need to invoke various computational tricks to create gathers (e.g., Jones, 2014).

Deriving parameters for migration: 1D versus 3D assumptions

Let us first consider the derivation of isotropic laterally invariant 1D P-wave velocity. When performing conventional velocity analysis on a common-midpoint (CMP) gather, we create a "velocity spectrum" (a form of Radon transform) by fitting traveltime trajectories to the observed CMP data (e.g., Al-Chalabi, 2014). However, the underlying assumptions behind this approach (shown in Figure 1) are that

- a single analytic function can be fitted across all offsets, whether that be a second-order hyperbolic fit or a higher-order ("anisotropic") nonhyperbolic fit; in other words, there is no lateral change in parameter values across the offset range recorded
- the subsurface reflectors are flat lying, thus the reflection points are positioned vertically below the CMP location (i.e., the earth is one-dimensional)

When there is lateral subsurface parameter change (whether this be velocity or structural dip), this 1D earth assumption is inappropriate, and the true reflection point no longer coincides with the common midpoint (Figure 2). In addition, migration algorithms that set out to handle lateral parameter variation (depth migrations) require the parameters to be in their true subsurface

locations and not arbitrarily posted vertically below the analysis points.

To achieve this, we have to analyze parameter information for each offset independently, effectively looking back along each 3D raypath to assess which parts of the subsurface have been traversed by energy arriving at a given receiver. This requires a tomographic inverse solution. For example, in a ray-based reflection-tomographic approach, we would perform ray tracing though a starting model and compare computed traveltimes with observed traveltimes (Figure 3). The word *tomography* itself derives from the Greek from *tomo* ("slice" or "cut") and *graph* ("to draw"). In other words, we describe the structure of an object based on a collection of slices through it.

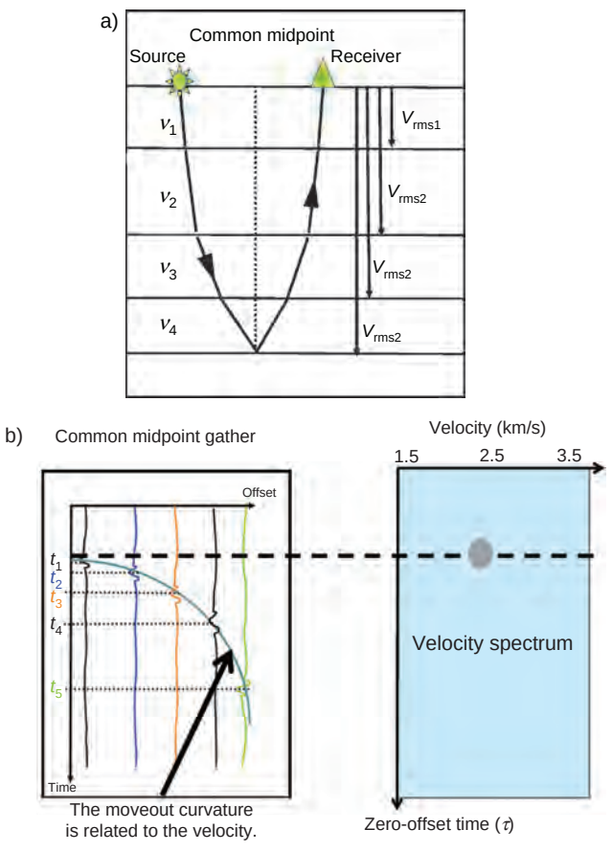

Figure 1. (a) For flat-lying strata with no lateral velocity change, the reflection point is below the midpoint. (b) For several source-receiver pairs, forming a CMP gather, we have a traveltime measurement for each source-receiver offset. In this case, we can fit a curve with a single representative parameter ($V_{\text{maximum-coherence}} = V_{\text{stacking}} \sim V_{\text{RMS}}$) for isotropic media and with two parameters V_{NMO} and η_{eff} (which characterizes the deviation from purely hyperbolic moveout) for anisotropic media. The maximum-coherence best-fit curves can be represented in the hyperbolic-Radon transform domain as a "velocity analysis spectrum," shown on the right.

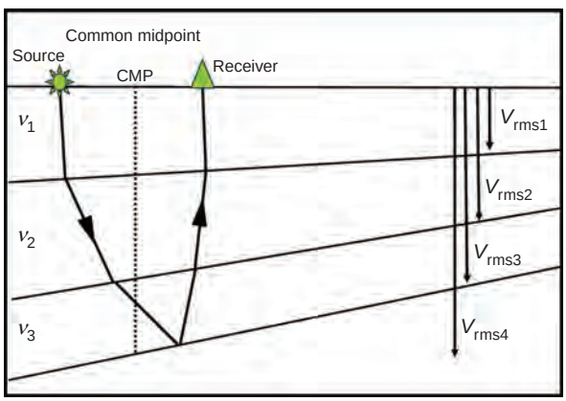

Figure 2. For dipping layers, the refection point is laterally shifted from the midpoint.

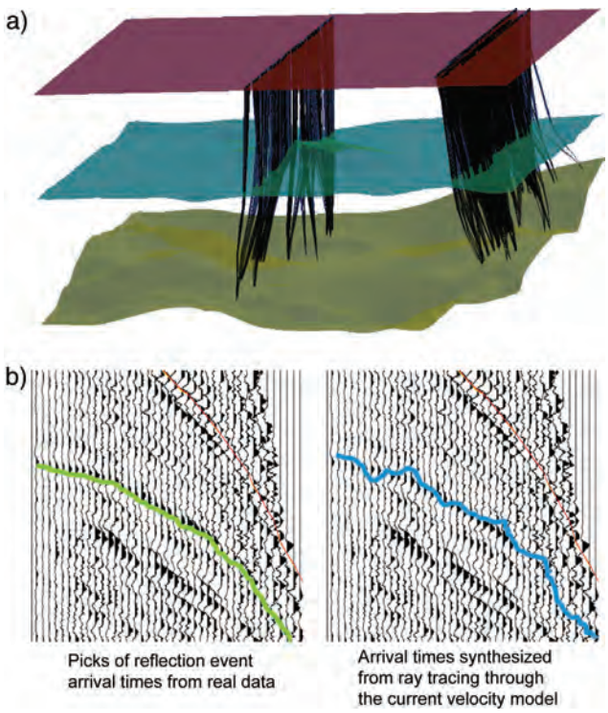

Figure 3. An inversion scheme can be developed to iteratively update the model by minimizing the differences between the observed and computed traveltimes for all gathers and all reflectors. (a) Ray tracing through the current model to estimate traveltimes associated with each offset for a reflecting horizon. (b) Comparison of actual and computed traveltimes for the horizon.

Inversion

Inversion deals with the mathematics of describing a thing based on measurements or observations that are associated with that thing. For example, consider some observed output data, d, associated with a model, m (that we want to know about), where the observed data result from some process associated with the model. With certain assumptions about the behavior of this process, namely, that there is a linear relationship between the model and the process, we can then write

$$d = Gm, \tag{1}$$

and the model recovered from the inversion process would thus be

$$m = G^{-1}d. \tag{2}$$

Backus and Gilbert (1968) and Backus (1970) give a formal description of this procedure in the context of inverse theory applied to geophysical observations.

In general, the parameters of the model and the observed data are described by a string of values (in vector form), and the operator G is described by a matrix. With p observations (i.e., d is a vector of length p) describing a model of n variables (i.e., m is a vector of length n), then G will be a matrix of size (p × n). If G is a square matrix (i.e., p = n) and some other conditions are met, then it is possible to directly determine the matrix G^{-1}, which is the inverse of G. However, in general, p is not equal to n, and other techniques must be employed to obtain a usable inverse of G to estimate the desired model parameters (e.g., Gerard T. Schuster, personal communication, 2015).

In addition, the available data are often noisy, inconsistent, and/or unreliable. Consequently, an entire branch of mathematics has evolved dealing with attempts to estimate a model based on the "interpretation of inaccurate, insufficient, and inconsistent data" (e.g., the work of that title by Jackson, 1972).

In the specific case of traveltime measurements made in a surface-seismic experiment, by which we are trying to determine the velocity structure of the earth, we have a particular inverse problem in which the measured data d are represented by a vector of two-way traveltimes measured for sound waves emanating from a source, propagating through the earth and reflecting off a horizon, then returning to an individual receiver. We will have one of these two-way traveltime measurements for each offset recorded and for every reflecting horizon that we pick in the data. To preserve measured traveltimes during any subsequent averaging processes, we invert for slowness (1/velocity) rather than for velocity (averaging velocity does not preserve traveltime because time is proportional to 1/velocity).

The velocity model m thus is described in terms of a vector of slownesses s (e.g., Claerbout, 2004). One could consider a 3D subsurface volume divided into a large number of perhaps rectangular model cells with a constant slowness in each cell. These individual cell slownesses are the model parameters, m, that we want to find. G is a matrix of path lengths that the rays traverse in each cell of the velocity model (Figure 4), which depend on the location of the sources and receivers on the surface. In other words, the G matrix describes the geometry of the problem.

The arrival time for raypath ABC for the fifth offset shown in Figure 4 for a source at location

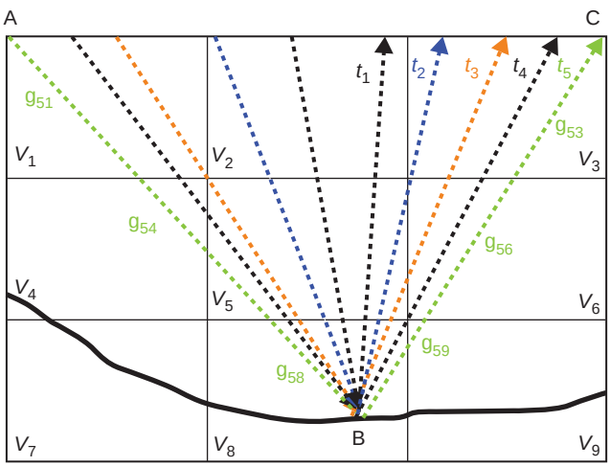

Figure 4. For a CMP gather, we have many arrival-time measurements for a given subsurface reflector element. Each source-to-receiver travel path can be decomposed into its elemental contributions from each cell (note that element g_{58} is V-shaped because it includes the reflection point). Each raypath will not be a straight line but will refract at each grid-cell boundary and might also be curved. Traveltimes autopicked on the real data gathers will be compared with the ray-trace computed traveltimes at each iteration. Ambiguity in traveltime measurement can arise, for example, from errors in wavelet phase or receiver location.

A and a receiver at location C, for the raypath reflecting off the dipping surface at B, comprises contributions from the travel paths g_{ij}, through each of the boxes traversed, such that:

$$\text{Total time for this offset, } t_5 = g_{51}/v_1 + g_{54}/v_4 + g_{55}/v_5 + g_{58}/v_8 + g_{59}/v_9 + g_{56}/v_6 + g_{53}/v_3, \quad (3)$$

where v_i is the interval velocity in the ith cell.

The solution to this particular inverse problem, as solved using reflection traveltime tomography, is dealt with by Lo and Inderwiesen (1994) as well as by Riabinkin et al. (1962), Bishop et al. (1985), Lines and Treitel (1985), Sword (1986), Etgen (1988), Stork (1992), Wang et al. (1995), Kosloff et al. (1996), Sexton (1998), Lambaré (2004), and Gray (2014), among many others.

The tomography algorithm iterates so as to minimize the arrival-time difference between the real observed data and synthetic forward-modeled data. This might be done for all locations on all layers simultaneously or layer by layer in a top-down manner. Within the tomography algorithm, there will typically be dozens of such iterations, each involving a new forward-modeling exercise. Unfortunately, there will always be many slightly different models that could equally well yield forward modeling that matches the observed field data (the issue of nonuniqueness), and the inversion might converge on a local minimum which is not truly representative of the real earth structure, although this latter problem can be mitigated with various schemes.

Hence, one important conclusion to draw from inverse theory is that there is never a correct answer and never can be. At best, we can obtain only models that adequately explain the observed data. This uncertainty is a manifestation of the principle of nonuniqueness in inverse theory.

So if you ask, "Is the model right?", then you are asking the wrong question.

Estimating image uncertainty

Given that we can never obtain a "correct" model based on measured data, we need to assess how suitable the derived approximate model is. It transpires that this is an extremely difficult task to undertake in a quantitative manner. There are certain minimum acceptance criteria, which tell us that at least the derived model explains the observed data, namely, flat image gathers following migration with the obtained model, which also match all available well data (at least to within some specified acceptance threshold).

Putting error bars on images is another issue. Many workers have attempted this over the years, and there are two broad approaches to accomplishing this task. First, we can assess the measured residual moveout in the final migrated image gathers, after a comprehensive model-building exercise, which usually would involve several iterations of ray or waveform tomography. Then, using an estimate to the inherent measurement uncertainty in the residual moveout (RMO) measurements (e.g., Ashton et al., 1994; Al-Chalabi, 1997; Chen and Schuster, 1999; Tom Armstrong, personal communication, 2008; Jones, 2010), many dozens of slight perturbations are introduced into the RMO values, with a distribution bounded by the estimated uncertainty (and the distribution of uncertainty might be further bounded by picked horizons).

For each of these slight RMO perturbations, a tomographic inversion is run so as to update the velocity model. This yields an ensemble of possible realizations of the velocity model, each of which is consistent with the observed data, to within the uncertainties associated with our measured RMO. Then for a specified target horizon, map demigration is performed (just once), followed by successive map migrations for each of these velocity models, giving rise to a spatial distribution of possible positions for each specified picked reflector.

Map migration is an approximate migration technique whereby a time horizon is picked from, say, a stacked section, and then, in conjunction with an interval velocity field, Snell's law is used to reposition this horizon to its equivalent depth location. This in effect delivers a low-cost emulation of a full-depth migration. Map demigration is the reverse procedure, converting a depth horizon picked from a prestack depth-migrated (preSDM) image to the corresponding (perhaps multivalued) time horizon positions.

Such methods of assessing structural uncertainty have been described by Cognot et al. (1995), Thore and Hass (1996), Thore and Juliard, (1999), Thore et al. (2002), and Letki et al. (2013). Bachrach (2010) discusses similar methods for anisotropic parameter uncertainty estimation.

The second approach is more esoteric, involving the mathematics of inversion used within

the tomographic solvers, dealing with what is called the model-resolution matrix. This can be used to assess the uncertainty associated with each of the inverted parameter values, but it still needs to be used in conjunction with something such as a map migration to assess the effect on image position (e.g., Jackson, 1972; Menke, 1989; Berryman, 1997, 2001; Chiţu et al., 2008; Etgen, 2008; Osypov et al., 2008; Jones, 2010).

Resolution scale length

If we intend to use sound to image the subsurface, then we first need a mathematical description of how sound propagates. This can be done using either ray theory or wave theory.

Ray theory is a gross simplification of describing how waves propagate, but it is sufficient if the sound's wavelength is small compared with the objects we are illuminating. Essentially, ray theory considers the behavior of points on the expanding sound wavefront and monitors their progress as the wavefront expands into the earth. Observing an individual point on the wavefront for all propagation times and then joining together this set of individual points forms a ray. Ray theory tells us which direction the wave is propagating in and how long it takes to reach a given point.

Velocity variation can be classified on the basis of the scale length of its lateral variation in comparison with the wavelength of the seismic wavelet. If the velocity scale length is much greater than the seismic wavelength, then ray-based tomography using only traveltime information can resolve the features. If not, then this high-frequency ray-based approach is inappropriate because diffraction behavior will predominate, and waveform tomography (also referred to as full-waveform inversion, or diffraction tomography), which uses the wavelet amplitude information, must be used instead.

One way of understanding this distinction is to consider two nearby bits of dirt on a reflecting horizon. If the wavelength of the sound impinging on this horizon is significantly smaller than the separation of the pieces of dirt, then as the sound wave refracts through this horizon, the vibrational behavior of these "dirt molecules" (Larson, 1995) is likely to be independent of each other. In this case, when the sound frequency is high, it makes sense to describe the refraction of a theoretical ray at each location as being totally independent. However, if the wavelength is comparable to the separation, then the vibrational behavior at points along that region of the reflector will not be independent, and the simple refraction description of sound transmission will be inappropriate.

Figure 5a shows a situation in which there is a velocity anomaly whose physical dimensions are much larger than the seismic wavelength. In this case, describing the propagating wavefront with representative rays normal to the wavefront (for the isotropic case) is acceptable because Snell's law adequately describes the refractive and reflective behavior at the interfaces of the anomalous velocity region.

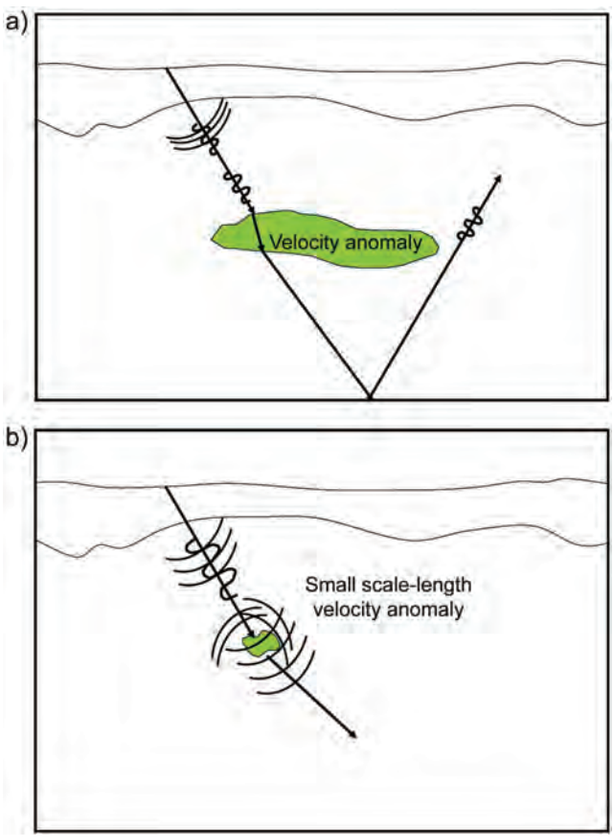

Figure 5. (a) A seismic wavelength that is much smaller than the anomaly we are trying to resolve. The propagating wavefront can be described adequately by raypaths. (b) A seismic wavelength that is larger or similar to the anomaly we are trying to resolve. The elements of the velocity feature behave more like point scatterers, producing secondary wavefronts. Trying to describe the propagation behavior as "rays" obeying Snell's law is no longer appropriate. After Jones (2010), Figures 11 and 12. Used by permission.

Conversely, once the velocity anomaly is of similar scale length to the seismic wavelet, as shown in Figure 5b, then diffraction behavior dominates because scattering is governing the position of the wavefronts. In this case, rather than just considering the arrival times of the events, we use the wave equation to estimate how the waveform will propagate through a given model, starting with some initial guess of the model.

Whereas traveltime tomography is iterated with renditions of ray tracing, with waveform tomography, we must iterate with renditions of the propagating waveform using repeated forward modeling with, for example, finite-difference code, which is expensive (e.g., Tarantola, 1984; Worthington, 1984; Pratt et al., 1996; Pratt et al., 2002; Pratt, 2003; Sirgue and Pratt, 2004; Warner et al., 2010).

Using a starting guess of the model, we perform an acoustic, or elastic, finite-difference modeling exercise for a limited bandwidth to make a synthetic version of the recorded shot data. The real and synthetic modeled data are subtracted, and the tomography iterates to update the gridded velocity model so as to minimize this difference. In principle, this technique can resolve features smaller than the seismic wavelengths available in the recorded data because phase and amplitude changes are very sensitive to slight variations in velocity.

Given that we can use either of these two possible ways of describing sound propagation (rays or waves) and that we could work with either raw unmigrated data or migrated data, we will have four possible ways of framing a tomographic problem. Table 2 summarizes these four basic possibilities for performing tomographic inversion for velocity model building. Because tomography using the full waveform is a rapidly developing field, the terminology is still evolving. Hence we might find different names in the literature. Full-waveform tomography has already been used for many years in global seismology, but its application to the more ambitious goal of resolving detailed sedimentary structure is relatively recent.

Generic model-building loop for ray-based tomography

When building a parameter model of the subsurface, we need to select a way of representing the information. Generally, models can be represented by layers, grids, or combinations of both (e.g., Billette et al., 2002). For older rocks in which sedimentary interfaces delimit changes in the velocity field, the geology "lends itself" to a layer-based model representation. In other words, the reflectivity is influenced greatly by the velocity contrast at the layer boundaries.

Conversely, in geologically younger environments in which the velocity regime might be decoupled from sedimentation and be more influenced by vertical compaction gradients controlled by dewatering, with isovelocity contours subparalleling the seabed, a gridded approach to velocity model building might be a better way to represent the subsurface.

However, a layer-based approach can miss subtle variation within layers, and a purely gridded approach might be unable to preserve rapid velocity variations. Moreover, for layers with very low impedance contrasts or poorly illuminated regions with significant velocity contrasts, we still need to constrain the model with interpretational input. With this in mind, many contemporary model-building schemes use gridded parameter fields in conjunction with picked horizon constraints at major velocity boundaries.

Whereas the initial model usually will have a smooth sediment velocity field, a detailed interpretation of the water bottom (for marine data) and surface topography (for land data) is

Table 2. Types and domains of tomography.

	Data domain	Migrated (or image) domain
Ray based	Refraction first-arrival tomography (e.g., for statics) Reflection-traveltime tomography Crosswell tomography	PreSTM tomography PreSDM tomography
Waveform based	Full-waveform inversion (a.k.a. wavefield tomography, waveform tomography, waveform inversion) Diffraction tomography	Wave-equation migration velocity analysis (WEM-VA) Wavepath tomography

incorporated. For marine data, we can use an initial preSDM using the water-velocity profile and pick the seabed reflector from this preSDM volume.

The information used to build the initial smooth sediment model often comes from time-domain information such as picked time horizons, stacking velocity fields, interval velocities (if available), vertical compaction gradients (or well information from which to derive them), and anisotropic parameter estimates (if available). From this initial time model, a starting depth model is derived after appropriate editing and smoothing of the initial information and incorporation of the surface or seabed topography.

At this juncture, if we are using ray-based tomography, we commence an iterative preSDM model update. After each iteration of migration, outputting common-reflection-point (CRP) gathers (perhaps on a 50 m × 50 m grid), a continuous locally coherent event autopicker is used to track residual moveout in the offset or angle domain over the 3D volume. This autopicking of RMO might be second order, fourth order, or nonparametric (generalized) moveout (GMO). The dip field, residual moveout, and coherency estimates are used as input to the tomography, after various quality-control (QC) steps.

Figure 6a shows a generic update loop for ray-based preSDM model building. Terminology can be confusing here also. We have a common-reflection-point gather or common-depth-point gather only if the velocity model used was correct. In the early stages of model building, the gathers certainly do not have the same image or depth points, but it is probably an unnecessary complication to introduce different terminology here. I have used CRP throughout this article for a gather emerging from depth migration; such gathers also are referred to as common-image gathers (CIGs) or common-image-point (CIP) gathers.

Figure 6b shows the nature of the moveout behavior after migration. If the gathers are flat, then at each offset, the reflection event appears at the same depth, and traces can be stacked to form an acceptable image. If the reflection events in the gathers curl upward at far offsets, then the migration velocity was too low (the far-offset reflection events did not travel a sufficient number of meters per second). If the events in the gather curl downward, then the velocity is too high.

The tomographic update indicated in Figure 6a strives to adjust migration velocities until all events in all gathers appear acceptably flat across the offset range used.

Typical QC steps include checking to ensure that nonparametric picking is correctly tracking complex moveout with gathers; remnant multiples have not been picked by the RMO picker; picked structural dips are not corrupted by aliasing for steep events; only events with high coherence are being used in the tomography; picked parameter fields are not "stripy looking" (acquisition bias needs to be removed); tomographic updates are not unacceptably oscillatory; tomographic residual error has dropped enough; resulting CRP gathers are flat and tie well markers; structural bias (pull-up and push-down) has been removed; and interval velocity profiles match those of available wells.

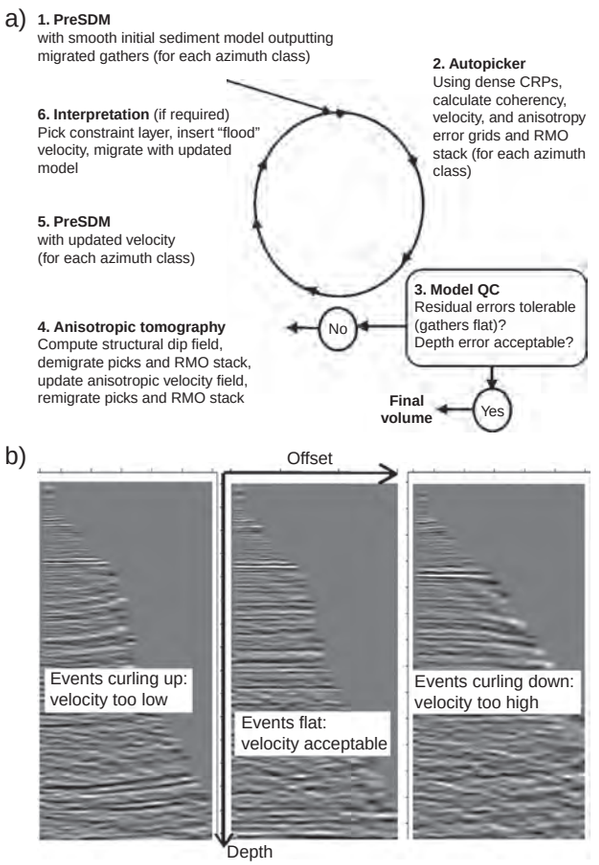

Figure 6. (a) Generic ray-based preSDM velocity update loop. (b) Behavior of reflection events in a preSDM CRP gather. Events curl upward when the velocity is too low and downward when the velocity is too high.

The overall strategy is to try to resolve the long-wavelength velocity structure in the early iterations (perhaps using a tomography cell size of $600 \times 600 \times 400$ m), and as the model is iteratively refined, to reduce cell size so as to extract the maximum resolution available from the data. This will depend on data quality, available fold, maximum offset, azimuthal distribution, frequency content, and so forth. For good-quality data, especially in deep water where we have good fold of coverage in the near-seabed sediments, cell sizes of perhaps $100 \times 100 \times 20$ m are reasonable for resolving shallow structure. However, for deeper structures, where we have a poor offset-to-depth ratio and thus velocity resolution is poor, we might revert to a larger tomographic cell or to nontomographic parameter scanning techniques.

Parametric versus nonparametric autopicking

For moderately complex media, it is practical to characterize the RMO behavior by fitting a smooth second- or fourth-order moveout trajectory to the reflection events in the migrated CRP gathers. However, for shorter-wavelength velocity variation (on a scale length of a few hundred meters), nonparametric picking is preferred (Hardy and Jeannot, 1999; Brittan and Yuan, 2005; Luo et al., 2014). Such generalized moveout behavior permits us to better characterize residual moveout anomalies, thus permitting the back propagation of residuals in the tomography to better localize the velocity anomalies that gave rise to these RMO features (e.g., Lambaré, 2002; Hardy, 2013; Fruehn et al., 2014).

Wide-azimuth and multiazimuth data

When we have wide-azimuth (WAZ) field data, we can use offset-vector tiles (OVT) as the input data sort order (e.g., Vermeer, 1998; Cary, 1999). In this case, autopicking for a ray-based tomography might work directly with the OVT 3D gathers so as to perform nonsectored picking. This procedure enables us to determine if there is any azimuthal variation in measured sound speed (perhaps resulting from near-vertical fracturing with a preferred orientation) so as to produce representative V_{fast} and V_{slow} RMO fields (and an associated azimuth) for input to the tomography.

For multiazimuth (MAZ) data, RMO picking is performed independently using conventional 2D picking tools for each acquisition azimuth, and then the tomography inverts all those RMO fields simultaneously so as to update a common model. It should be noted that the tomographic engine itself does not change; it is only the way we bin and pick RMO information that changes. The tomographic solver should always ray-trace from the actual source and receiver positions so it will honor the locations of whatever data we give it. However, if we have only narrow-azimuth (NAZ) data, we will be less able to resolve heterogeneity in the earth structure because we will have poorer ray coverage and distribution in 3D space than with WAZ or MAZ data.

Anisotropic model building

In general, for an elastic solid, there are 21 constants that govern elastic wave propagation. These are not readily measureable from surface-seismic data, so we attempt to classify wave motion using various combinations of them, such as P-wave and S-wave speeds and other parameters related to anisotropic elastic wave propagation. Our description of anisotropic behavior often relates to a simplified model in which we assume that there is no change in wave speed as a function of azimuth with respect to some polar axis (the transversely isotropic [TI] case).

The TI description can be extended to include fractures with a specified orientation, most simply the orthorhombic description, in which we can have two orthogonal fracture sets, both of which are also perpendicular to the structural bedding plane. Extending this description to incorporate fractures with arbitrary orientations could perhaps be achieved in an elastic migration scheme (Grechka, 2014), but inverting to estimate all 21 elastic parameter is beyond current capabilities.

In anisotropic media, it generally is observed that well velocities are lower than seismic velocities (because the seismic raypaths sample more of the horizontal sound-speed direction, which is commonly the fastest in layered media). Thus, the depths from an isotropic depth migration are generally greater than the corresponding well depths (exceptions to this could be when we have vertical fractures in a layer or when the lateral stress field dominates propagation behavior, compared with layering effects). Consequently, it is not proper to migrate isotropically using the well velocities because this will give rise to poorly focused images and improperly collapsed diffractions.

However, in the TI case, if we migrate anisotropically, we will take into account the deviation between well and seismic velocities via the anisotropy parameters. Using a higher-order picker, we can attempt to estimate fourth-order moveout effects, usually characterized by the effective-eta (η_{eff}) parameter (Alkhalifah and Tsvankin, 1995; Alkhalifah, 1997; Grechka and Tsvankin, 1998).

As with RMS velocity being inverted to interval velocity, η_{eff} can be inverted to yield the interval η values for each layer. The η parameter, in conjunction with V_{NMO}, is used for time migration.

For depth migration, we also need to account for depth calibration, which then requires a velocity term plus at least two other parameters. In the simplest case, this can be achieved using a depth-calibration term, delta (δ), in conjunction with a term, epsilon (ε), related to differences between horizontal and vertical velocity (Thomsen, 1986).

In Thomsen's notation, the vertical and horizontal velocities are related to the surface seismic near-offset interval velocity (V_{NMO}) by

$$V_{\text{NMO}} = V_v\sqrt{1+2\delta} \approx V_v(1+\delta), \tag{4}$$

and

$$V_h = V_v\sqrt{1+2\varepsilon} \approx V_v(1+\varepsilon), \tag{5}$$

where V_{NMO} is the near-offset interval velocity estimated from stacking velocity analysis, V_v is the vertical velocity seen in well logs, and V_h is the horizontal component of velocity (which we do not usually have access to but which in principle could be measured from crosswell experiments).

In other words, the velocity measured from surface-seismic data is higher than the earth's vertical velocity component (for positive δ). Hence, an isotropic depth migration using this higher seismically derived velocity will produce an image that appears too deep in comparison to well markers. In addition, because V_h is generally larger than V_v, ε should be positive (although from a purely theoretical viewpoint, it could be negative).

The higher-order moveout seen on NMO-corrected or isotropically migrated gathers does not explicitly give us access to ε and δ. The η value derived from measured higher-order moveout η_{eff} is related to Thomsen's ε and δ parameters by

$$\eta = (\varepsilon - \delta)/(1+2\delta), \tag{6}$$

$$V_h = V_{\text{NMO}}\sqrt{1+2\eta} \approx V_{\text{NMO}}(1+\eta). \tag{7}$$

These parameters are interval quantities specified for each distinct layer and can vary spatially within a layer.

To determine the δ parameter (which primarily governs near-vertical propagation), we usually need well control or vertical-seismic-profiling (VSP) data. The values for δ for each layer can be estimated from the well thicknesses H_w and isotropic seismic migration thicknesses H_s:

$$\delta \approx (H_s - H_w)/H_w. \tag{8}$$

In the case of TTI (transversely isotropic material with a tilted axis), we should endeavor to measure the thicknesses in the well and the seismic data along the well track rather than assuming verticality. If we have a VSP corridor stack, then we can perform continuous correlation between the VSP stack and the corresponding preSDM data so as to form a continuous δ function estimate.

For TTI (as opposed to VTI [polar anisotropy with a vertical axis]), the estimation of ε is more complex. The flat-layer assumptions made in a simplistic approach will no longer hold for steeply dipping layers, and a full tomographic solution or a scanning approach will be needed. TTI tomography usually inverts for velocity along the polar axis V_0 and ε (based on information from a higher-order autopicker or a depth-error versus depth curve from a VSP stack).

In principle, we can also invert for δ if we have multidip layer constraints, but in practice, we usually rely on well calibration to estimate δ. In general, the change in velocity with angle α from the polar axis is given by

$$V(\alpha) \approx V_0(1+\delta\cos^2\alpha\sin^2\alpha+\varepsilon\sin^4\alpha). \tag{9}$$

For a vertical polar axis (i.e., VTI), $V_0 = V_v$.

The polar axis for TTI anisotropy usually is taken as being equivalent to the geologic structural axis, but this is a questionable assumption (Jones and Davison, 2014).

It is possible to start the model-building procedure anisotropically "from scratch," but this usually requires very dense well control and reliably picked layers to bound the anisotropic

regions and/or some preliminary detailed analysis of seismic data around the well locations. Alternatively, we can commence the model building isotropically so as to attempt to accommodate vertical velocity gradients before comparing well and seismic layer thicknesses (or interval velocity trends) to estimate δ.

In the case of a ray-tracing migration algorithm such as Kirchhoff, the sound speed used for each ray would differ as a function of direction. In the initial model-building route for anisotropic migration, we thus reduce the isotropically derived seismic velocities by scaling with the δ parameter to bring them into line with the range of well velocities.

In general, we do not attempt to invert for all three TTI parameters (because they are too closely coupled) but rather invert sequentially first for velocity and thereafter for ε or perhaps for both these parameters simultaneously (depending on data quality and user preference). Inversion for δ is more questionable because we have little constraint on it resulting from scarcity of well control. The dip field itself ideally should constitute another inversion parameter, but it is often not inverted for but simply adjusted at each iteration (either by repicking the 3D dip field on the latest image or by successive map demigration/remigration of key horizons).

Azimuthal anisotropy might also need to be considered, especially if we have near-vertical fractures (the HTI and orthorhombic cases; e.g., Zdraveva, 2012) and/or significant heterogeneity (e.g., Jenner, 2008, 2011). However, to assess such anisotropy, we need to input data with substantial azimuthal coverage for a wide range of offsets (e.g., Schapper et al., 2009).

In this case, we can extend the TTI description to an orthorhombic paradigm, requiring the introduction of more parameters. Environments where such fractures might be important include the sediment layers distorted over salt canopies and fracture carbonate reservoirs. Estimation of attributes related to fracture openness and orientation is of great interest for reservoir characterization, so the usefulness of this information extends beyond model building and imaging.

Anisotropic prestack depth migration in the absence of well control

To reliably estimate the δ parameter, we need well control in addition to surface reflection-seismic data. However, it often is noted that in shaley media, there is a reasonably stable relationship between ε and δ (typically, ε varies from about 1.5 to 2.0 times δ; e.g., Vernik and Liu, 1997). Hence, in the absence of well control, if we can reliably measure the higher-order moveout effects from the long offsets in the seismic data, we could assert a relationship between ε and δ and use that.

In this case, we use second- and fourth-order (or nonparametric) automatic picking to estimate velocity and η RMO. Thence we use the fixed relationship between ε and δ to reduce the tomographic solution to a two-parameter problem and invert for velocity and ε, keeping the fixed ε:δ relationship.

Resolving near-surface anomalies

Seismic wavefields encounter near-surface structure on the way to a deeper reflector and on the way back up to the receivers. Hence, if velocity anomalies are missing from the migration model, the resulting image will be distorted unacceptably. These distortions will be encountered at the source location for the downgoing energy and at the receiver locations for the upcoming reflected energy. Therefore, as the acquisition spread moves across the survey, the width of the disturbed zone will be equal to the cable length plus the geobody width (plus a Fresnel zone because we are dealing with wavefronts rather than hypothetical rays). Hence, although the unresolved geobody itself might be only a few hundred meters wide, the associated subsurface distortion will be several kilometers wide (e.g., Armstrong, 2001; Armstrong et al., 2001).

The nature of the problem is outlined with simple synthetic data derived from the model shown in Figure 7a, where a low-velocity geobody is present at the seabed in shallow water. Figure 7b shows the 3550-m offset plane after normal moveout with a smooth background velocity field (without the low-velocity geobody) and the NMO-corrected CMP gather.

The shallow section is absent because it falls within the mute zone, but an important point is that the distortion caused by the channel appears not below the anomaly location (CMP 2442), but rather, symmetrically to either side of it. The CMP gather from location 2300, where the distortion appears for this offset plane, shows the distortion (pushed down) at offset 3550 m. Midpoints to either side of the anomaly are perturbed, as indicated by the two raypaths on the

offset plane (Figure 7b). However, the appearance of the anomaly in the final migrated image will depend on the interplay of mute, AVO, and migration velocity, as seen in Figure 8.

Here, in a preSDM using the smooth background model, the anomaly manifests as a pushdown immediately below the channel in the shallow section and as a pair of distortions to either side of the channel in the deeper section. If we had included the channel feature in the preSDM velocity model correctly, the distortion would be removed, producing a correct subsurface image.

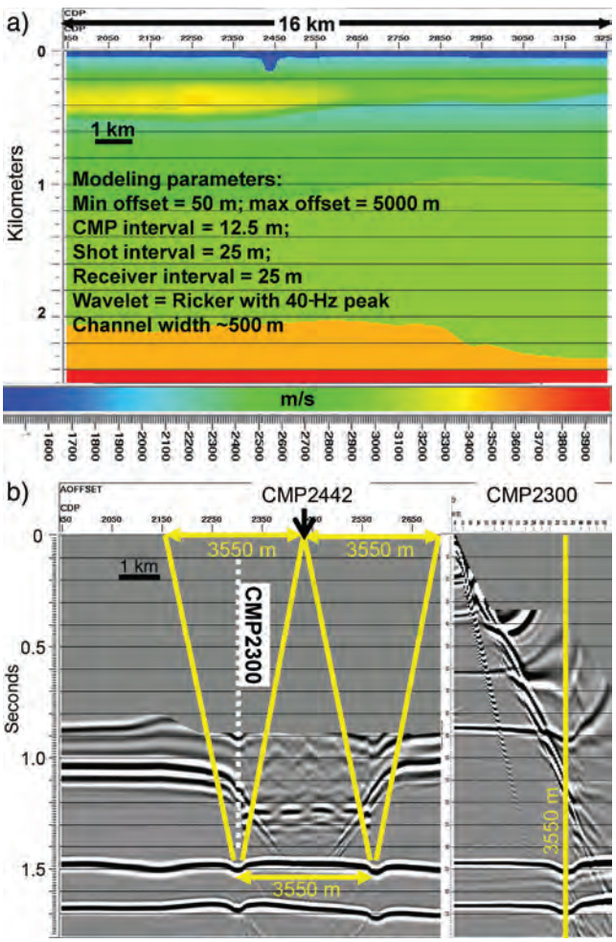

Figure 7. (a) Interval velocity model for synthetic data, with low-velocity channel at the seabed. (b) Far-offset sections from the data after NMO with a smooth, manually picked velocity function. Distortion caused by the channel persists to each side of the channel over a distance of more than half the offset used. On the right is a CMP gather (maximum offset 5 km) from the side of the channel (CMP location 2300) showing the pushdown on offset 3550 m.

Jones (2012) gives a comprehensive overview of building preSDM velocity models for marine near-surface velocity anomalies.

Figure 9 displays a real data example from the North Sea showing essentially these same features. Here, the near-surface channel (in this instance, with high velocity fill) could be resolved by tomographic inversion or by manual picking. In the figure, the results are shown for velocities derived via tomography but constrained by manual picking of the geobody (Jones, 2012).

In very shallow water, overcorrected refractions, seabed multiples, and direct arrivals often obscure near-surface channels, making it difficult to pick the features on an image or discern moveout behavior in low-fold data. For this type of 3D data, the geometry and fill velocity of the channel features could be derived by mapping the channel imprint on a deeper reflector. The imprint effect is estimated by subtracting a smoothed and unsmoothed surface, picked on a preSDM image created using a smooth background velocity model, without any channel features. This forms a 3D geobody that will be used to represent the near-surface channel by placing this object in the model at or near the seabed. Its size and fill velocity are adjusted until the resulting migrated image is free from distortion (e.g., Jones, 2012).

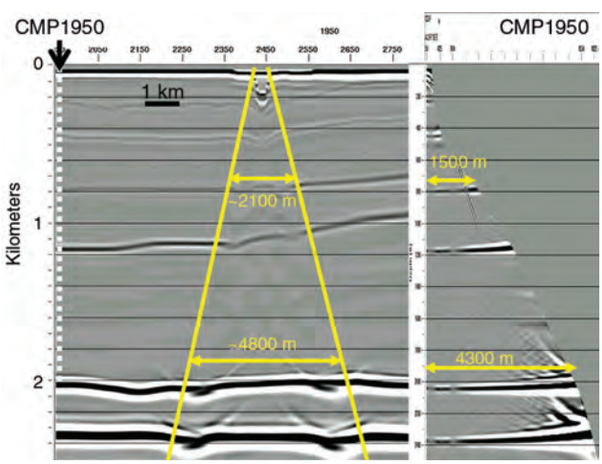

Figure 8. Stacked section for a maximum offset of 5 km after preSDM using a velocity model without the channel feature. The gather from the unperturbed far left of the section (CMP 1950) indicates the available offset range with depth, after muting. The image distortion has a lateral extent related to the available offset range. At 2-km depth, the available offset range in the CRP gather is 4300 m, and the subsurface distortion is spread over about 4800 m.

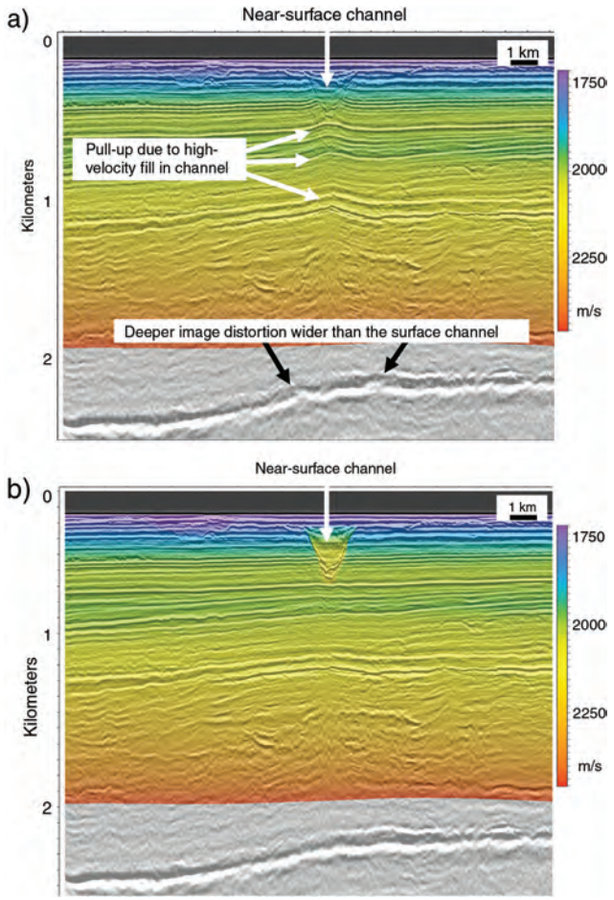

Figure 9. (a) Shallow-water high-velocity channel causing pull-up on 3D Kirchhoff preSDM using smooth velocity model. (b) 3D Kirchhoff preSDM after manual picking of the channel and a velocity determined by tomography helps to resolve the laterally widespread deeper image distortion. The symmetrical deeper distortions are removed. After Jones (2012), Figure 9. Used by permission.

It should be noted that both NMO-corrected and prestack time migrated (preSTM) data, even with the "correct" velocity model, will exhibit the pushdown distortion because neither can deal correctly with a velocity anomaly with a short spatial wavelength. In other words, both NMO and preSTM make the assumption that all traces in a CMP gather should be processed with the same 1D velocity-time function pertaining to the CMP location. The actual velocity function provided to the process might change laterally, but at any given CMP, traces from all offsets in the gather are treated as if they propagated in the same laterally invariant velocity field.

These observations underline the fact that there is no such thing as a "correct" preSTM velocity model; we can only obtain a compromise between ignoring lateral velocity change while trying to flatten reflection events in a CMP gather. The consequence is that image distortion in preSTM remains below velocity anomalies. The only way to remove such image distortion is by using preSDM with an appropriate velocity model.

The next example concerns rapid velocity variation from deepwater offshore Sri Lanka (Fruehn et al., 2014). In this area, the seafloor is incised with deep canyons, and the sedimentary sequence below them shows clear evidence of the presence of buried paleocanyons containing significant lateral velocity variation in comparison with the surrounding sediments. The short-wavelength velocity variation associated with the buried canyons will limit the ability of ray-based tomographic inversion to resolve the required level of complexity if the autopicking being used was parametric (in other words, if it tried to fit simple second- or fourth-order curves to the complex moveout).

Figure 10 shows CRP gathers from 3D anisotropic Kirchhoff preSDM from the two approaches. Overall, the CRP-gather flatness is significantly improved for the deeper major reflectors by using nonparametric picking. Gathers after conventional parametric update show sinuous RMO behavior typical of unresolved overburden short-wavelength lateral velocity anomalies. Following nonparametric update, sinuosity is removed to a large extent, resulting in simpler RMO behavior.

Figure 11 shows the final Kirchhoff 3D preSDM image in the zone with paleocanyon complexity after several iterations of parametric picking as compared with the corresponding image after four iterations of nonparametric moveout picking. Overall, the image is improved significantly for all deeper major reflectors, and velocity features of just a few hundred meters in width are resolved. In this example, the smallest tomography cell size used was $150 \times 150 \times 25$ m.

Picking constraint layers

When we have significant velocity variation (perhaps > 1.5 times change in velocity) on a scale length less than the tomography cell size, then picked horizon constraints can be useful in model building. Picking horizons as constraints in a grid-based tomography is referred to sometimes as hybrid, or hybrid-gridded, tomography.

For example, Figure 12 shows the top chalk horizon overlying the Silverpit crater in the North Sea. Here, the chalk surface displays circular corrugations with a peak-to-peak distance of several hundred meters. In this case, the tomographic cell size ($600 \times 600 \times 400$ m) was too coarse to resolve such lateral and vertical variation, and a picked constraint layer was used to constrain the model (Evans et al., 2005). Using a purely gridded velocity model suffers from an imprint of the unresolved top-chalk structure at the base-chalk horizon (Figure 13a) and deeper structures. Inserting a picked constraint layer at the top chalk resolves this problem, as shown in Figure 13b.

Salt

Such manual picking is usually inevitable where salt tectonics is involved, for a variety of reasons. The velocity contrast at the salt interface is often large; the topography of the salt is usually too rugose for ray methods to work well (both tomography and migration); the internal layered (flow) structure and velocity distribution within the evaporite body is usually very poorly understood and perhaps unresolvable (Jones and Davison, 2014); and scattering can render through-salt ray tracing impractical.

Hence, salt model building tends to be more of a manual exercise than a simple tomographic model update. Once the overburden velocities are determined by tomography, we pick the top salt (usually on an RTM image) and then populate the velocity model below the top-salt pick

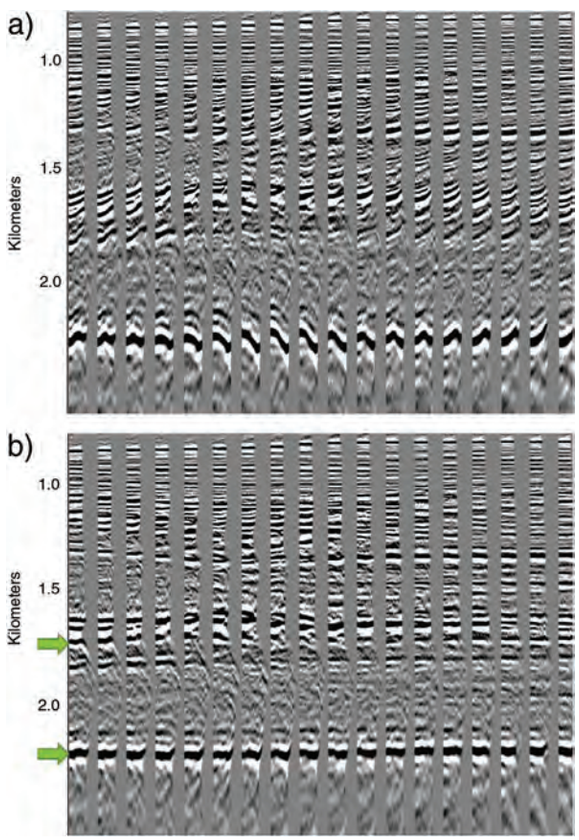

Figure 10. (a) 3D PreSDM CRP gathers in the zone with paleocanyon complexity after several iterations of parametric picking (5-km maximum offset). (b) After four iterations of nonparametric moveout picking, the result is improved. Overall CRP gather flatness is improved significantly for these deeper major reflectors. After Fruehn et al. (2014), Figure 3.

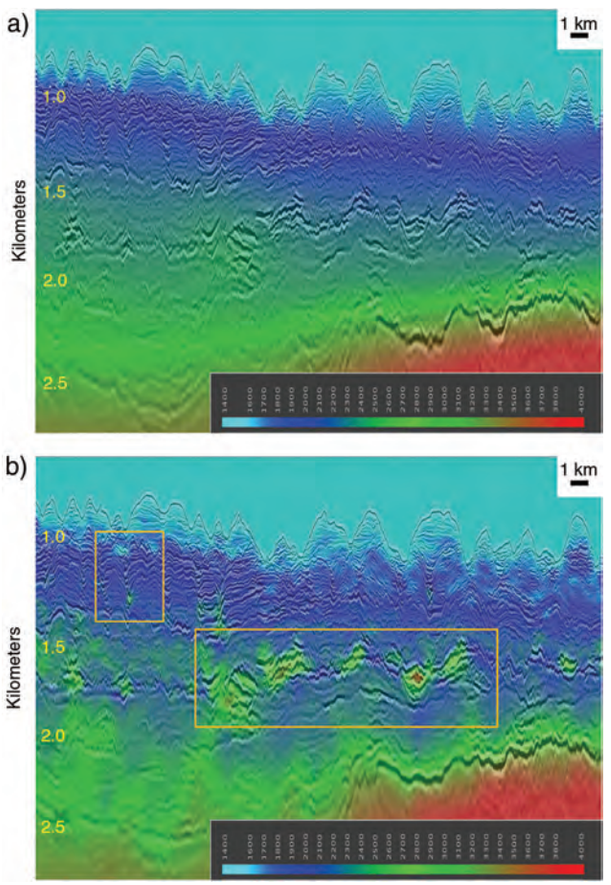

Figure 11. (a) Final Kirchhoff 3D preSDM image in the zone with paleocanyon complexity after several iterations of parametric picking, with interval velocity overlay. (b) Corresponding image after four iterations of nonparametric moveout picking. Boxes indicate areas where higher-resolution velocity information has been recovered. Overall, the image is improved for all deeper major reflectors. After Fruehn et al. (2014), Figure 4.

with a representative velocity ("flooding") and migrate to image the base salt (again, with an RTM algorithm). This process can be repeated and adjusted several times to refine the salt, and salt velocities can be adjusted to cater for inclusions ("dirty-salt" models) or internal evaporite structures (e.g., the SEG subsalt imaging special edition of GEOPHYSICS, Leveille et al., 2011).

Converted-mode reflections from the base salt can be exploited sometimes to help delineate the base salt (e.g., Lewis, 2006). These reflections will have a different angular coverage than P-wave reflections, so they sometimes can illuminate parts of the base salt not seen in the P-wave data. This is achieved by performing a preSDM with a velocity model using S-wave velocity within the salt body. The assumption is that we have P-wave propagation to and from the top salt, with conversion to shear occurring at the top salt, such that we have shear propagation within the salt body itself. Given that the salt shear-wave velocity is usually about half that of the P-wave velocity, any potential base-salt shear images could perhaps be seen in previous "sediment-flood" iterations, thereby giving an indication as to whether a shear-velocity flood is worthwhile.

When we have a velocity inversion below the salt, which is often the case, the angular coverage of reflections from subsalt reflectors is usually very poor; hence, velocity resolution is compromised severely. In addition, upcoming raypaths from deeper reflectors often can undergo postcritical reflection at the base salt; hence, we do not receive much upcoming energy (e.g., Cao and Brewer, 2013).

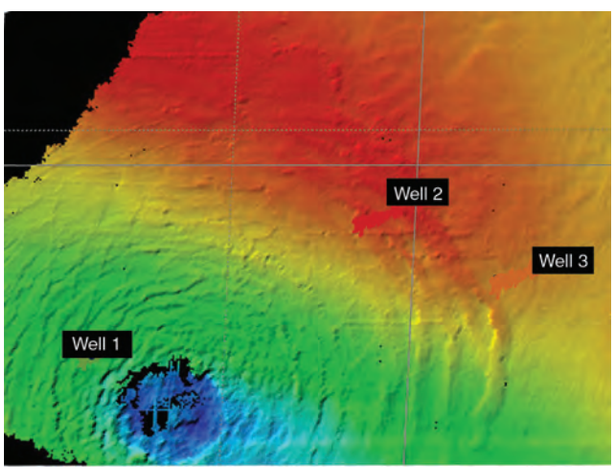

Figure 12. Top chalk horizon, picked as the first "hard" layer constraint for the hybrid tomography. Concentric rings associated with the craterlike structure are visible in the lower left. After Jones et al. (2007), Figure 7.

Stress-induced effects

If we have a salt weld, where the salt thickness has thinned to almost zero at the base-salt horizon, there can be a pronounced increase in vertical stress because of the comparative lack of buoyant uplift compared to adjacent salt pillows. This tends to increase the seismic velocity in the

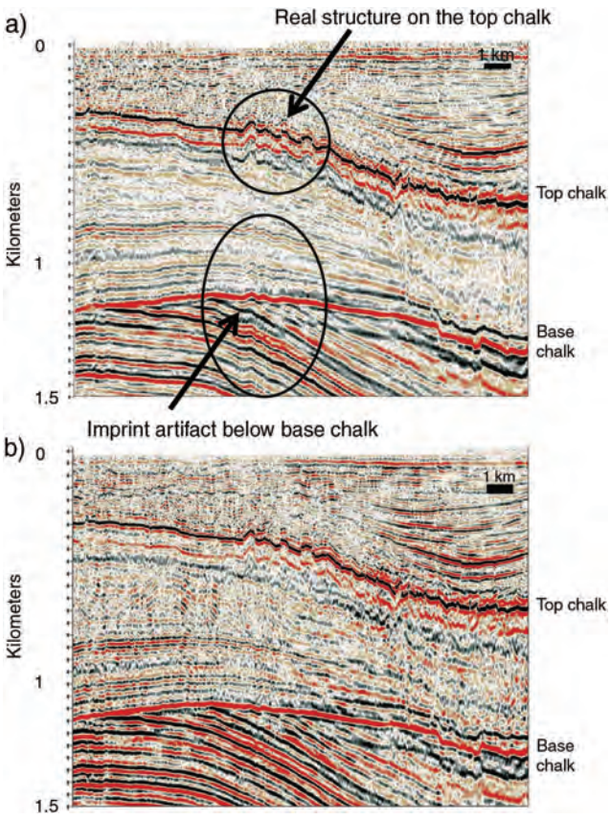

Figure 13. (a) Inline depth section, intersecting well location 1 from the purely gridded tomographic model. The corrugations on the top chalk associated with the craterlike feature are clearly visible. Below these corrugations, we see an imaging artifact resulting from velocity smearing through the top chalk. (b) Inline depth section, intersecting well location 1 from the hybrid gridded model. The corrugations on the top chalk associated with the craterlike feature are still clearly visible. However, the imprint of those corrugations below the top chalk has been removed, producing a more reasonable image.

sedimentary strata locally just above the weld (e.g., Hoetz et al., 2011), but this detail might not be accounted for adequately in the depth-migration velocity model. The velocity used in the migration will therefore be too low in the vicinity of the weld, and underlying structures will be pulled up on migrated sections (Jones and Davison, 2014).

In addition to the stress effects in the sediments overlying and adjacent to the salt body, we have the possibility of anomalous behavior below the salt because of reduction in overburden stress caused by buoyancy effects, lowering seismic velocities in comparison with neighboring outboard sediments with the same depth of burial (e.g., Sengupta and Bachrach, 2008; Petmecky et al., 2009). Reduction in velocity also can be observed in overpressured shales (e.g., Ritter, 2010). Such stress-induced effects, summarized in Figure 14, can increase or decrease sediment velocity by about 15% (e.g., Petmecky et al., 2009; Hoetz et al., 2011).

In addition to salt-induced stress effects, we have the more general field of geomechanical modeling, in which the effects of sediment loading and regional stress variation can be incorporated into a model to help predict or constrain a velocity field (e.g., Birdus, 2008; Herwanger and Koutsabeloulis, 2011).

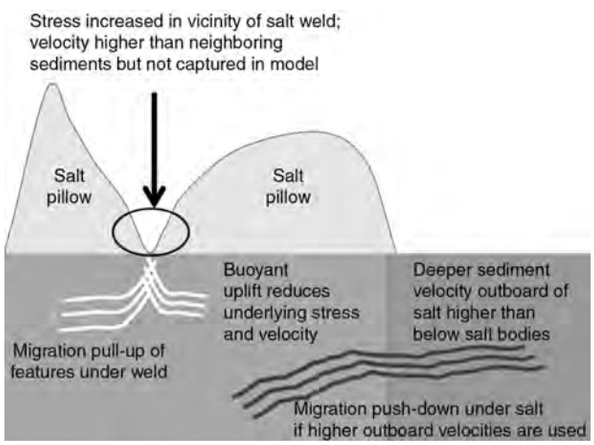

Figure 14. Velocity imprint of stress regimes in the vicinity of salt. We have pull-up (undermigration) of features below a salt weld if the sediment velocity above the weld is too low. We have pushdown (overmigration) of features below a salt pillow if the higher outboard sediment velocities are extrapolated under the salt without compensating for the effects of salt buoyancy (which will reduce the velocity).

Land environments: Topography and statics

For land data, several factors introduce traveltime distortions to what would otherwise be smooth moveout trajectories in gathers. Rapidly varying elevation introduces trace-to-trace jitter, as do near-surface velocity variations caused by such things as weathered zones, karstic voids, and dunes. In addition, if the surface is not horizontal, then even for a constant-velocity medium, the moveout behavior in CMP gathers is not hyperbolic, so velocity analysis and other 2D transform-based processes such as Radon and τ-p filters are compromised. Hence, for conventional data preprocessing and NMO velocity analysis, we have to apply various static time-shift corrections at the source and receiver, which are typically surface-consistent, and at CMP locations, in an attempt to make moveout behavior look locally more hyperbolic (e.g., Zhu et al., 1992; Cox, 1999).

Figure 15 summarizes the different sources of statics for a land environment. On the left of the figure, we note a locally flat floating datum specific to each individual CMP gather (the blue line in Figure 15) designed to make moveout behavior look more hyperbolic. The near-surface model static shift for each trace in a CMP is made up of high spatial frequency (HF) surface-consistent components at both the source and receiver locations, which result from any rapid topographic variations and any rapid near-surface velocity variation, plus a low spatial frequency (LF)

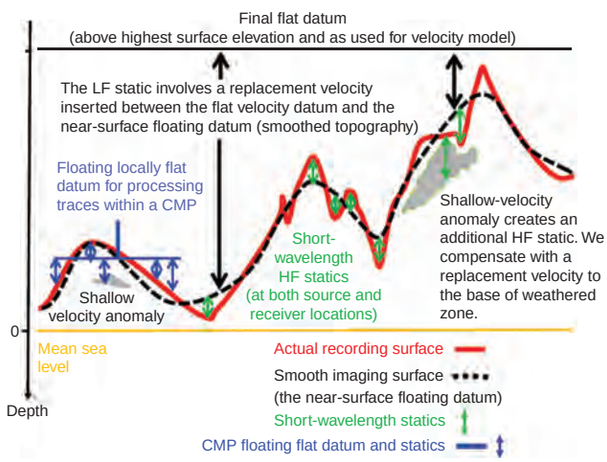

Figure 15. Some sources of statics in the near surface of land data. After Jones (2010), Figure 8. Used by permission.

CMP-consistent component to shift all traces in the CMP from their shot and receiver elevations to a common flat processing datum at the CMP smooth floating datum elevation.

The LF static component can be derived from refraction analysis, perhaps resulting from tomographic inversion of first-arrival picks. For near-surface velocity variation, i.e., the weathered zone, we typically shift traces to the base of the weathered zone with the weathering velocity and then back to the surface with a replacement velocity. When the HF and LF statics have been applied, there might still be some very high spatial-frequency jitter (VHF) which can be removed using residual static techniques.

It is also preferable to have all traces output from the processing to be of the same length, referenced to a common origin; hence, times will be referenced to an overall flat datum. During preprocessing, this might be an intermediate flat datum at some average elevation. However, for the final output from a depth-migration project, it will in many cases be a final flat velocity-datum plane above the highest point of the topography, with a constant replacement velocity between it and the near-surface floating datum, which is a smooth version of the actual topography. The depth-migration algorithm itself will migrate from the smooth near-surface floating datum, and then following the migration, the data would be referenced to the flat final-velocity datum plane.

In the marine environment, we also can have static effects between sail lines, resulting from tidal, water temperature, and salinity variations.

For prestack migration, we can ray-trace or downward-continue from the near-surface floating datum and thus can incorporate some of the surface features in the velocity model. Therefore, we do not need to apply all these static corrections. We still might want to apply statics for prestack migration, in both time and depth, and this will depend on the lateral scale length of the near-surface velocity anomalies.

If, for example, the near-surface velocity anomalies are smooth enough to be handled properly by the migration, then we should incorporate them in the migration velocity model and not as static corrections. For smooth surface topography, we could migrate the data as they stand, without the need for static correction. If, however, the topography varies rapidly and/or we are unable to incorporate near-surface velocity anomalies into the velocity model, then a static treatment still will be required to shift the data to the smooth near-surface datum (the black dashed line in Figure 15).

Whereas time migration cannot deal with lateral velocity anomalies of less than a cable length in width, depth migration can cope with such heterogeneity, except for very small-scale velocity or topography anomalies. These still might need to be addressed with a static solution (indicated by green arrows in Figure 15).

If the surface elevations of the shots and receivers are handled correctly, then as with near-surface velocity anomaly effects, there should be no imprint of the topographic relief on the deeper seismic image. Thus, for land data, just as we need to quality-control marine data using the near-offset channels, we need to ensure that there are no remnant pull-up or pushdown distortions on the deeper parts of the image that resemble the surface topography. This quality control might be performed by creating a map of the arrival times or rms amplitude distribution on a deep horizon and comparing these with the near-surface features, such as topography and/or channel distributions, to highlight any remnant imprints on the image.

Unfortunately, a mismatch between what has been done in preprocessing and what is to be done in migration can easily occur, giving rise to false structure in the final image. For example, if there are some near-surface effects that are treated as a static in preprocessing but are to be incorporated as a velocity feature in depth migration, then we must ensure that the preprocessing component of this static is removed prior to the migration. Otherwise, we will account for geologic effects twice.

Waveform inversion

The methods outlined so far have either been based on ray theory, whose lateral resolution is limited by the Fresnel zone to perhaps a few hundred meters, or have been based on some seriously limiting assumptions, which produce very approximate solutions. To move beyond these methods, we need a technique that can better estimate the small-scale velocity distribution in the near surface, and waveform inversion is intended to do this. Waveform inversion, also referred to as waveform tomography or full-waveform inversion (Table 2), has the potential

to deliver accurate and precise estimates of near-surface velocity structure at a scale length similar to the wavelength of the seismic data (e.g., Pratt, 2003; Warner et al., 2010; Brittan et al., 2013). As indicated in Figure 5, more conventional ray-based tomographic techniques are limited in their resolving power to several times the wavelength of the recorded waves.

In ray-based tomography, we iteratively forward-modeled just the arrival times of events, but with waveform methods, we attempt to forward-model the full waveform and hence incorporate amplitude, wavelet phase, and arrival times. Ideally, we also would like to include all source-generated effects including surface waves, but current implementations restrict the analysis to only transmitted and reflected body waves (energy traveling within the solid earth and not along the surface). Consequently, any surface-wave energy must be removed prior to waveform inversion.

It was noted in the description of ray tomography that we might have dozens of iterations within the tomographic solver. The same is true for waveform inversion. The computational cost associated with iterative forward modeling of a full elastic wavefield is high, and as a consequence, current methods are limited in what they set out to achieve. In addition, it can be shown that the convergence rate of such iterative procedures depends on both the lowest available frequency and on how close the starting model is to the true model (Symes, 2008; Plessix et al., 2010; Shah et al., 2012; Symes and Huang, 2014; W. W. Symes, personal communication, 2015).

Moreover, although we might have a good initial estimate of V_P (usually coming from some ray-based tomographic inversion), we need to question how we could obtain reasonable starting estimates of V_S, density, Q, and any anisotropic parameters.

Given that most current industrial implementations (at the time of this writing, July 2015) make an acoustic approximation (ignoring density changes), we have a serious problem in trying to invert using reflection data. In ignoring density changes, we will obtain an inaccurate estimation of the wavelet amplitude, which will manifest itself as a velocity error when the waveform tomography tries to match the modeled amplitudes against the real data by adjusting the velocity. Hence, we need to find those components in the data which are less sensitive to density, and refractions satisfy this requirement. However, refractions penetrate only to a depth of perhaps one-third to one-fourth of the cable length and therefore facilitate model updates only in the shallow part of the seismic section. To obtain any meaningful penetration depth, we need long offsets.

However, any velocity error in the starting model commonly manifests itself on the farthest offsets as cycle skipping, which is difficult but not impossible to avoid in inversion. This leads to the problem of falling into local minima (Warner at al., 2013). The simplest way to mitigate cycle skipping is to work with a low-frequency waveform, which has little oscillatory structure and therefore few side lobes to confuse the matching process.

As a result of the above requirements, at least for waveform inversion in the data domain (Table 2), we need long offsets and low frequencies for contemporary schemes to converge reliably (Plessix and Perkins, 2009; Vigh et al., 2009; Sirgue et al., 2010; Wang et al., 2011). Inversion using wave-equation migration velocity analysis (WEM-VA) is a bit less restrictive in that being based on reflection events in the migrated data, it can resolve deeper anomalies, albeit perhaps more smoothly varying. However, with increase in computer power, we can afford more iterations, and in addition, we can forward-model with more representative schemes, including Q, anisotropy, and density. We then might obtain more robust models and benefit from making use of deeper reflection events (because once we include density contrast, the modeled amplitudes of the reflection events will be more reliable). However, unless we also use multicomponent data, the null space of the inversion is likely to increase.

Another technique of increasing interest is surface-wave inversion (note that the waveform-inversion schemes already mentioned deal with seismic body waves traveling in the solid earth, and not surface waves). Here, the high-amplitude ground-roll events that plague land and ocean-bottom cable (OBC) data recordings are exploited in an attempt to estimate near-surface properties, primarily shear velocities. By analyzing the dispersion behavior for various propagation modes, S-wave velocity estimates can be obtained for the first few hundred meters below the surface (e.g., Socco et al., 2010; Douma and Haney, 2011).

Nontomographic update

There are cases in which tomography experiences difficulties in updating the velocity model. These are usually when the signal-to-noise ratio is too poor to reliably pick moveout error or when we suffer from a low offset-to-depth ratio and thus have poor velocity resolution. Even for waveform inversion, some parameters can be poorly constrained (e.g., anisotropy), and a scanning method is still of use.

In these cases, velocity-perturbation image scanning can be used, whereby a scan of preSDM imaged sections or suites of CRP gathers are produced for a series of lines and/or crosslines. Each member of the scan corresponds to a migration produced with a slight perturbation of the velocity model and/or the anisotropy parameters. Picking velocity updates from these scans yields a very powerful interpretational tool for constraining the velocity update in difficult areas. This image-scanning technique can be applied via perturbations imposed either from the surface, for Kirchhoff and WEM migration methods, or from just below some horizon (e.g., base salt, base permafrost, and so forth) in the WEM case (e.g., Wang et al., 2006).

Conclusions

To produce a reliable image of the subsurface, we must use a depth-migration scheme. However, to do this, we require a detailed model of the parameter fields for use by the migration. In the most complete contemporary viscoacoustic case, these parameter fields include V_p, structural dip axes, orthorhombic anisotropy parameters, and Q. Moving beyond this simplification (albeit complex) to a fuller rendition of the elastic strain tensor with 21 independent components is unlikely to occur.

Obtaining reliable values of all these parameters for the full 3D volume to be imaged is perhaps impractical, so we make various simplifying assumptions. Even with such assumptions, inverting for a wide range of parameters given a limited and inconsistent data set is challenging. In the best-case scenario, ray-based tomography supplemented with waveform inversion can yield a suitable model. However, we often still need to fall back on various bespoken techniques requiring manual intervention to incorporate detailed velocity anomalies in the migration model.

In their current form, industrial model-building techniques are iterative, requiring several rounds of migration, tomography, and event picking, typically taking several months to provide a model for a large seismic survey.

Acknowledgments

My thanks go to the various cited colleagues who have given permission to use their figures in this review article and to ION GX Technology for permission to publish this work. My thanks also go to Vladimir Grechka, Bin Wang, John Brittan, Nick Bernitsas, Dave McCann, Jacques Leveille, Tony Martin, and the SEG reviewer for their helpful comments.

References

Al-Chalabi, M., 1997, Parameter nonuniqueness in velocity versus depth functions: Geophysics, **62**, no. 3, 970–979, http://dx.doi.org/10.1190/1.1444203.

Al-Chalabi, M., 2014, Principles of seismic velocities and time-to-depth conversion: EAGE.

Alkhalifah, T., 1997, Velocity analysis using nonhyperbolic moveout in transversely isotropic media: Geophysics, **62**, no. 6, 1839–1854, http://dx.doi.org/10.1190/1.1444285.

Alkhalifah, T., and I. Tsvankin, 1995, Velocity analysis for transversely isotropic media: Geophysics, **60**, no. 5, 1550–1566, http://dx.doi.org/10.1190/1.1443888.

Armstrong, T., 2001 Velocity anomalies and depth conversion — Drilling success on Nelson field, Central North Sea: 63rd Conference and Exhibition, EAGE, Extended Abstracts, IV-2.

Armstrong, T. L., J. McAteer, and P. Connolly, 2001, Removal of overburden velocity anomaly effects for depth conversion: Geophysical Prospecting, **49**, no. 1, 79–99, http://dx.doi.org/10.1046/j.1365-2478.2001.00238.x.

Ashton, C. P., B. Bacon, C. Déplanté , D. T. Sinclair, G. Redekop, 1994, 3D seismic survey design: Oilfield Review, **6**, no. 2, 19–32.

Bachrach, R., 2010, Applications of deterministic and stochastic rock physics modeling to anisotropic velocity model building: 80th Annual International Meeting, SEG, Expanded Abstracts, 2436–2440, http://dx.doi.org/10.1190/1.3513342.

Backus, G., 1970, Inference from inadequate and inaccurate data: Proceedings of the National Academy of Sciences of the United States of America, **65**, 100–105.

Backus, G., and F. Gilbert, 1968, The resolving power of gross earth data: Geophysical Journal of the Royal Astronomical Society, **16**, no. 2, 169–205, http://dx.doi.org/10.1111/j.1365-246X.1968.tb00216.x.

Berkhout, A. J., 1982, Seismic migration: Imaging of acoustic energy by wave field extrapolation, Part A: Theoretical aspects, Elsevier, http://store.elsevier.com/Seismic-Migration-Imaging-of-Acoustic-Energy-by-Wave-Field-Extrapolation__/A_-J_-Berkhout/isbn-9780444602008/.

Berryman, J. G., 2001, Computing tomographic resolution matrices using Arnoldi's iterative inversion algorithm: SEP, Report 82, 1–176.

Berryman, J. G., 1997, Resolution for Lanczos and Paige-Saunders inverses in tomography: SEP, Report 77, 1–185.

Billette, F. J., J. T. Etgen, and W. E. Rietveld, 2002, The key practical aspects of 3D tomography — Data picking and model representation: 64th Conference and Exhibition, EAGE, Extended Abstracts, B006.

Birdus, S., 2008, Restoring velocity variations below seafloor with complex topography by geomechanical modeling: 78th Annual International Meeting, SEG, Expanded Abstracts, 3310–3314, http://dx.doi.org/10.1190/1.3064032.

Bishop, T. N., K. P. Bube, R. T. Cutler, R. T. Langan, P. L. Love, J. R. Resnick, R. T. Shuey, D. A. Spindler, and H. W. Wyld, 1985, Tomographic determination of velocity and depth in laterally varying media: Geophysics, **50**, no. 6, 903–923, http://dx.doi.org/10.1190/1.1441970.

Brittan, J., J. Bai, H. Delome, C. Wang, and D. Yingst, 2013, Full waveform inversion — The state of the art: First Break, **31**, 75–81.

Brittan, J., and J. Yuan, 2005, Dense multi-offset reflection tomography: 75th Annual International Meeting, SEG, Expanded Abstracts, **24**, 2534–2537, http://dx.doi.org/10.1190/1.2148239.

Cao, J., and J. D. Brewer, 2013, Critical reflection illumination analysis: Interpretation, **1**, no. 1, T57–T61, http://dx.doi.org/10.1190/INT-2013-0031.1.

Cary, P. W., 1999, Prestack imaging with 3-D common-offset-vector gathers: CREWES Research Report, **11**.

Chen, J., and G. T. Schuster, 1999, Resolution limits of migrated images: Geophysics, **64**, no. 4, 1046–1053, http://dx.doi.org/10.1190/1.1444612.

Chiţu, D. A., M. N. Al-Ali, and D. J. Verschuur, 2008, Assessing estimated velocity-depth models: Finding error bars in tomographic inversion: Geophysics, **73**, no. 5, VE223–VE233, http://dx.doi.org/10.1190/1.2951469.

Claerbout, J. C., 2004, Earth soundings analysis: Processing versus inversion: Stanford University, Stanford Exploration Project.

Cognot, R., P. Thore, and A. Haas, 1995, Tying seismic to well data using structural uncertainties: 64th Annual International Meeting, SEG, Expanded Abstracts, 494–497, http://dx.doi.org/10.1190/1.1932137.

Cox, M., 1999, Static corrections for seismic reflection surveys: SEG Geophysical Reference Series No. 9, http://dx.doi.org/10.1190/1.9781560801818.

Douma, H., and M. Haney, 2011, Surface-wave inversion for near-surface shear-wave velocity estimation at Coronation field: 81st Annual International Meeting, SEG, Expanded Abstracts, 1411–1415, http://dx.doi.org/10.1190/1.3627466.

Etgen, J. T., 2008, Applications of the model resolution matrix: 78th Annual International Meeting, SEG, Expanded Abstracts, Imaging Workshop, 3702–3703, http://dx.doi.org/10.1190/1.3064104.

Etgen, J. T., 1988, Velocity analysis using prestack depth migration: Linear theory: 58th Annual International Meeting, SEG, Expanded Abstracts, 909–912, http://dx.doi.org/10.1190/1.1892387.

Evans, E., M. Papouin, S. Abedi, M. Gauer, P. Smith, and I. F. Jones, 2005, Southern North Sea pre-SDM imaging using gridded tomography: 67th Conference and Exhibition, EAGE, Extended Abstracts, E011.

Fruehn, J., V. Valler, N. Stevens, S. Adhikari, M. Phani, S. Sarkar, C. G. Rao, P. Kumar, and P. Routray, 2014, Velocity model update via inversion of non-parametric RMO picks over canyon areas offshore Sri Lanka: 84th Annual International Meeting, SEG, Expanded Abstracts, 3070–3074, http://dx.doi.org/10.1190/segam2014-0050.1.

Gray, S. H., 2014, Seismic imaging and inversion: What are we doing, how are we doing, and where are we going?: 84th Annual International Meeting, SEG, Expanded Abstracts, 4416–4420, http://dx.doi.org/10.1190/segam2014-0292.1.

Grechka, V., 2014, Seismic characterization of fractured reservoirs: SEG Encyclopedia of Exploration Geophysics, http://dx.doi.org/10.1190/1.9781560803027.entry1.

Grechka, V., and I. Tsvankin, 1998, 3-D description of normal moveout in anisotropic inhomogeneous media: Geophysics, **63**, no. 3, 1079–1092, http://dx.doi.org/10.1190/1.1444386.

Hardy, P., 2013, Ongoing R&D in ray based tomography: Well worth the effort: 83rd Annual International Meeting, SEG, Expanded Abstracts, 4806–4810, http://dx.doi.org/10.1190/segam2013-0521.1.

Hardy, P., and J.-P. Jeannot, 1999, 3D reflection tomography in time-migrated space: 69th Annual International Meeting, SEG, Expanded Abstracts, 1287–1290, http://dx.doi.org/10.1190/1.1820744.

Herwanger, J., and N. Koutsabeloulis, 2011, Seismic geomechanics: How to build and calibrate geomechanical models using 3D and 4D seismic data: EAGE Education Tour 5.

Hoetz, G., J. Steenbrinkl, N. Bekkers, A. Vogelaar, and S. Luthi, 2011, Salt-induced stress anomalies: An explanation for variations in seismic velocity and reservoir quality: Petroleum Geoscience, **17**, no. 4, 385–396, http://dx.doi.org/10.1144/1354-079311-002.

Jackson, D. D., 1972, Interpretation of inaccurate, insufficient, and inconsistent data: Geophysical Journal of the Royal Astronomical Society, **28**, no. 2, 97–109, http://dx.doi.org/10.1111/j.1365-246X.1972.tb06115.x.

Jenner, E., 2011, Combining VTI and HTI anisotropy in prestack time migration: Workflow and data examples: The Leading Edge, **30**, no. 7, 732–739, http://dx.doi.org/10.1190/1.3609087.

Jenner, E., 2008, Data example and modelling study of P-wave azimuthal anisotropy potentially caused by isotropic velocity heterogeneity: First Break, **27**, no. 2, 45–50, http://dx.doi.org/10.3997/1365-2397.2009004.

Jones, I. F., 2010, An introduction to velocity model building: EAGE, http://dx.doi.org/10.3997/9789073781849.

Jones, I. F., 2012, Tutorial: Incorporating near-surface velocity anomalies in pre-stack depth migration models: First Break, **30**, no. 1821, 47–58, http://dx.doi.org/10.3997/1365-2397.2011041.

Jones, I. F., 2014, Tutorial: Migration imaging conditions: First Break, **32**, no. 12, 45–55. http://dx.doi.org/10.3997/1365-2397.2014017.

Jones, I. F., R. I. Bloor, B. L. Biondi, and J. T. Etgen, 2008, Prestack depth migration and velocity model building: SEG Geophysics Reprints Series No. 25, http://dx.doi.org/10.1190/1.9781560801917.

Jones, I. F., and I. Davison, 2014, Seismic imaging in and around salt bodies: Interpretation, **2**, no. 4, SL1–SL20, http://dx.doi.org/10.1190/INT-2014-0033.1.

Jones, I. F., M. J. Sugrue, and P. B. Hardy, 2007, Hybrid gridded tomography: First Break, **25**, no. 4, 35–41, http://dx.doi.org/10.3997/1365-2397.2007013.

Kosloff, D., J. Sherwood, Z. Koren, E. Machet, and Y. Falkovitz, 1996, Velocity and interface depth determination by tomography of depth migrated gathers: Geophysics, **61**, no. 5, 1511–1523, http://dx.doi.org/10.1190/1.1444076.

Lambaré, G., 2004, Stereotomography: Past, present and future: 74th Annual International Meeting, SEG, Expanded Abstracts, 2367–2370, http://dx.doi.org/10.1190/1.1845225.

Lambaré, G., 2002, The use of locally coherent events in depth processing: A state of the art: 72nd Annual International Meeting, SEG, Expanded Abstracts, 2261–2264, http://dx.doi.org/10.1190/1.1817163.

Larson, G., 1995, "First dirt molecule," "The Far Side" cartoon, ~~http://chemistry-batz.wikispaces.com/file/view/Far%20Side.First%20dirt%20molecule.jpg/503234216/300x384/Far%20Side.First%20dirt%20molecule.jpg,~~ accessed 18 September 2015.

Letki, L. P., H. Ben-Hadj-Ali, and P. Desegaulx, 2013, Quantifying uncertainty in final seismic depth image using structural uncertainty analysis — Case study offshore Nigeria: Extended Abstracts, First EAGE West Africa Workshop 2013: Subsurface Challenges in West Africa, http://dx.doi.org/10.3997/2214-4609.20131775.

Leveille, J. P., I. F. Jones, Z.-Z. Zhou, B. Wang, and F. Liu, 2011, Subsalt imaging for exploration, production, and development: A review: Geophysics, **76**, no. 5, WB3–WB20, http://dx.doi.org/10.1190/geo2011-0156.1.

Lewis, J. L., 2006, The potential of mode-converted waves in salt interpretation: Proceedings of the SEG/EAGE Summer Research Workshop.

Lines, L. R., and S. Treitel, 1985, Inversion with a grain of salt: Geophysics, **50**, no. 1, 99–109, http://dx.doi.org/10.1190/1.1441841.

Lo, T., and P. Inderwiesen, 1994, Fundamentals of seismic tomography: SEG Geophysical Monograph Series No. 6, http://dx.doi.org/10.1190/1.9781560802334.

Luo Z., J. Brittan, D. Fan, B. Mecham, P. Farmer, and G. Martin, 2014, Imaging complexity in the earth — Case studies with optimized ray tomography: The Leading Edge, **33**, no. 9, 1016–1022, http://dx.doi.org/10.1190/tle33091016.1.

Menke, W., 1989, Geophysical data analysis: Discrete inverse theory, rev. ed.: Academic Press, Inc., International Geophysics Series No. 45.

Osypov, K., D. Nichols, M. Woodward, O. Zdraveva, and C. E. Yarman, 2008, Uncertainty and resolution analysis for anisotropic tomography using iterative eigendecomposition: 78th Annual International Meeting, SEG, Expanded Abstracts, 3244–3249, http://dx.doi.org/10.1190/1.3064019.

Petmecky, R. S., M. L. Albertin, and N. Burke, 2009, Improving sub-salt imaging using 3D basin model derived velocities: Marine and Petroleum Geology, **26**, no. 4, 457–463, http://dx.doi.org/10.1016/j.marpetgeo.2009.01.011.

Plessix, R. E., and C. Perkins, 2009, 3D full-waveform inversion with a frequency-domain iterative solver: 71st Conference and Exhibition, EAGE, Extended Abstracts, U039.

Plessix, R.-E., G. Baeten, J. W. de Maag, M. Klaassen, R. Zhang, and Z. Tao, 2010, Application of acoustic full waveform inversion to a low-frequency large-offset land data set: 80th Annual International Meeting, SEG, Expanded Abstracts, 930–934, http://dx.doi.org/10.1190/1.3513930.

Pratt, R. G., 2003, Waveform tomography: Theory and practice: 12th International Workshop on Controlled-Source Seismology, http://www.geophys.geos.vt.edu/hole/ccss/prattCCSS.pdf, accessed 18 September 2015.

Pratt, R. G., F. Gao, C. Zelt, and A. Levander, 2002, A comparison of ray-based and waveform tomography — Implications for migration: 64th Conference and Exhibition, EAGE, Extended Abstracts, B023.

Pratt, R. G., Z.-M. Song, P. Williamson, and M. Warner, 1996, Two-dimensional velocity models from wide-angle seismic data by wavefield inversion: Geophysical Journal International, **124**, no. 2, 323–340, http://dx.doi.org/10.1111/j.1365-246X.1996.tb07023.x.

Riabinkin, L. A., I. V. Napalkov, V. V. Znamenskii, and I. N. Voskresenskii, 1962, Theory and practise of the CDR seismic method: Transactions of the Gubkin Institute of Petrochemical and Gas Production (Moscow).

Ritter, G., 2010, Interpretation driven velocity model building to improve subsalt imaging: 80th Annual International Meeting, SEG, Expanded Abstracts, 4098–4102, http://dx.doi.org/10.1190/1.3513716..

Robein, E., 2003, Velocities, time-imaging and depth-imaging: Principles and methods, EAGE, http://bookshop.eage.org/Webshop/product_details.aspx?prod_code=AA0052&cat_code=.

Schapper, S., R. Jefferson, A. Calvert, and M. Williams, 2009, Anisotropic velocities and offset vector tile prestack-migration processing of the Durham Ranch 3D, northwest Colorado: The Leading Edge, **28**, no. 11, 1352–1361, http://dx.doi.org/10.1190/1.3259614.

Sengupta, M., and R. Bachrach, 2008, Velocity updating around salt bodies using stress modeling solutions and non-linear elasticity: 78th Annual International Meeting, SEG, Expanded Abstracts, 3048–3052, http://dx.doi.org/10.1190/1.3063978.

Sexton, P. A., 1998, 3D velocity-depth model building using surface seismic and well data: Ph.D. thesis, University of Durham (SuperDix).

Shah, N., M. Warner, T. Nangoo, A. Umpleby, I. Stekl, J. Morgan, and L. Guasch, 2012, Quality assured full-waveform inversion: Ensuring starting model adequacy: 82nd Annual International Meeting, SEG, Expanded Abstracts, http://dx.doi.org/10.1190/segam2012-1228.1.

Sirgue, L., O. I. Barkved, J. Dellinger, J. Etgen, U. Albertin, and J. H. Kommedal, 2010, Full waveform inversion: The next leap forward in imaging at Valhall: First Break, **28**, no. 1728, 65–70, http://dx.doi.org/10.3997/1365-2397.2010012.

Sirgue, L., and R. G. Pratt, 2004, Efficient waveform inversion and imaging: A strategy for selecting temporal frequencies: Geophysics, **69**, no. 1, 231–248, http://dx.doi.org/10.1190/1.1649391.

Socco, L. V., S. Foti, and D. Boiero, 2010, Surface-wave analysis for building near-surface velocity models — Established approaches and new perspectives: Geophysics, **75**, no. 5, 75A83–75A102, http://dx.doi.org/10.1190/1.3479491.

Stork, C., 1992, Reflection tomography in the post-migrated domain: Geophysics, **57**, no. 5, 680–692, http://dx.doi.org/10.1190/1.1443282.

Sword, C. H. Jr., 1986, Tomographic determination of interval velocities from picked reflection seismic data: 56th Annual International Meeting, SEG, Expanded Abstracts, 657–660, http://dx.doi.org/10.1190/1.1892933.

Symes, W. W., 2008, Migration velocity analysis and waveform inversion: Geophysical Prospecting, **56**, no. 6, 765–790, http://dx.doi.org/10.1111/j.1365-2478.2008.00698.x.

Symes, W. W., and Y. Huang, 2014, Inversion velocity analysis: Computing an accurate gradient: 84th Annual International Meeting, SEG, Expanded Abstracts, Workshop 18.

Tarantola, A., 1984, Inversion of seismic reflection data in the acoustic approximation: Geophysics, **49**, no. 8, 1259–1266, http://dx.doi.org/10.1190/1.1441754.

Thomsen, L., 1986, Weak elastic anisotropy: Geophysics, **51**, no. 10, 1954–1966, http://dx.doi.org/10.1190/1.1442051.

Thore, P., and A. Haas, 1996, A practical formulation of migration error due to velocity uncertainties: 58th Conference and Exhibition, EAGE, Extended Abstracts, X016.

Thore, P., and C. Juliard, 1999, Fresnel zone effect on seismic velocity resolution: Geophysics, **64**, no. 2, 593–603, http://dx.doi.org/10.1190/1.1444566.

Thore, P., A. Shtuka, M. Lecour, T. Ait-Ettajer, and R. Cognot, 2002, Structural uncertainties: Determination, management, and applications: Geophysics, **67**, no. 3, 840–852, http://dx.doi.org/10.1190/1.1484528.

Vermeer, G. J. O., 1998, Creating image gathers in the absence of proper common-offset gathers: Exploration Geophysics, **29**, 636–642, http://dx.doi.org/10.1071/EG998636.

Vernik, L., and X. Liu, 1997, Velocity anisotropy in shales: A petrophysical study: Geophysics, **62**, no. 2, 521–532, http://dx.doi.org/10.1190/1.1444162.

Vigh, D., E. W. Starr, and J. Kapoor, 2009, Developing earth models with full waveform inversion: The Leading Edge, **28**, no. 4, 432–435, http://dx.doi.org/10.1190/1.3112760.

Wang, B., V. Dirks, P. Guillaume, F. Audebert, and D. Epili, 2006, A 3D subsalt tomography based on wave-equation migration-perturbation scans: Geophysics, **71**, no. 2, E1–E6, http://dx.doi.org/10.1190/1.2187720.

Wang, B., K. Pann, and R. A. Meek, 1995, Macro velocity model estimation through model-based globally-optimized residual curvature analysis: 65th Annual International Meeting, SEG, Expanded Abstracts, 1084–1087, http://dx.doi.org/10.1190/1.1887297.

Wang, C., H. Delome, C. Calderon, D. Yingst, J. Leveille, R. Bloor, and P. Farmer, 2011, Practical strategies for waveform inversion: 81st Annual International Meeting, SEG, Expanded Abstracts, 2534–2538, http://dx.doi.org/10.1190/1.3627718.

Warner, M., T. Nangoo, N. Shah, A. Umpleby, and J. Morgan, 2013, Full-waveform inversion of cycle-skipped seismic data by frequency down-shifting: 83rd Annual International Meeting, SEG, Expanded Abstracts, 903–907, http://dx.doi.org/10.1190/segam2013-1067.1.

Warner, M., A. Umpleby, I. Stekl, and J. Morgan, 2010, 3D full-wavefield tomography: Imaging beneath heterogeneous overburden: 72nd Conference and Exhibition, EAGE, Extended Abstracts, Workshop 6.

Worthington, M. H., 1984, An introduction to geophysical tomography: First Break, **2**, no. 1165, 20–26, http://dx.doi.org/10.3997/1365-2397.1984020.

Zdraveva, O., 2012, Anisotropic model building in complex media: VTI, TTI, or orthorhombic: Presented at the SEG/EAGE Summer Research Workshop.

Zhu, X., D. P. Sixta, and B. G. Angstman, 1992, Tomostatics: Turning-ray tomography + static corrections: The Leading Edge, **11**, no. 12, 15–23, http://dx.doi.org/10.1190/1.1436864.